Generative Adversarial Networks for the Inverse Design of Two-Dimensional Spinodoid Metamaterials

Sheng Liu*† and Pınar Acar‡
Virginia Tech, Blacksburg, 24061, VA, USA

The geometrical arrangement of metamaterials controls their mechanical properties, such as Young's modulus and shear modulus. However, optimizing the geometrical arrangement for user-defined performance criteria leads to an inverse problem that is intractable when considering numerous combinations of properties and underlying geometries. Machine learning techniques have been proven to be effective and practical to accomplish such non-intuitive design tasks. This paper proposes an inverse design framework using conditional generative adversarial networks (CGANs) to explore and optimize 2D metamaterial designs consisting of spinodal topologies, called spinodoids. CGANs are capable of solving the "many-to-many" inverse problem, which requires generating a group of geometric patterns of representative volume elements with target combinations of mechanical properties. The performance of the networks was validated by numerical simulations with the finite element method. The proposed inverse design framework vastly improves the efficiency of design exploration and optimization of spinodoid metamaterials.

Nomenclature

$\hat{C}_{ij}$	=	Second-order homogenized elastic modulus tensor
d	=	Direction in the Cartesian coordinates
D	=	Discriminator of the CGAN
E_{11}	=	Young's modulus in transverse direction
E_{22}	=	Young's modulus in longitudinal direction
G	=	Generator of the CGAN
G_{12}	=	Shear modulus
L_D	=	Loss of the discriminator
L_G	=	Loss of the generator

*Corresponding author, shengl20@vt.edu
†Graduate Research Assistant, Ph.D. Student, Department of Mechanical Engineering, AIAA Student Member
‡Assistant Professor, Department of Mechanical Engineering, AIAA Member

n = Non-uniform orientation

N = Number of the training data

S = Solver of the CGAN

S^2 = Two-dimensional sphere

x = Real microstructures from the database

X = Presence of materials

y_i = Actual properties

$\hat{y}_i$ = Predicted properties

z = Random noise vector from the latent space

ψ = Phase field

θ = Angle in Cartesian coordinate system

ϕ_0 = Porosity

$\omega^{(S)}$ = Parameters of the solver

$\omega^{(D)}$ = Parameters of the discriminator

$\omega^{(G)}$ = Parameters of the generator

$\overline{\sigma}_{ij}$ = Average stress

$\overline{\varepsilon}_{ij}$ = Average strain

I. Introduction

Cellular materials are attracting interest in various industries, including automotive [1], aerospace [2], and marine equipment [3]. This is owing to their lightweight feature with high stiffness and strength. In recent years, advances in additive manufacturing have allowed engineers to tailor the internal geometrical arrangement of cellular materials at the microstructural level and produce various kinds of cellular metamaterials, e.g., kirigami mechanical metamaterials inspired by the art of cutting and folding paper [4], flexible chiral metamaterials consisting of interlocked Archimedean spirals [5], and porous metamaterials with repeating star-shaped voids or pores [6]. However, the metamaterials involving microstructures defined as trusses, jointed connections, and sharp edges are subject to high-stress concentrations, leading to poor recoverability and unexpected mechanical behavior [7]. To overcome potential issues due to high-stress concentrations while maintaining outstanding mechanical performance, Kumar et al. [7] reported a new class of metamaterials formed by spinodal topologies called spinodoid metamaterials. These materials are naturally generated by a phase separation process known as spinodal decomposition [7]. Spinodoid topologies involve materials with continuous and smooth surfaces having approximately zero-mean curvature in their microstructures [7]. This makes spinodoid metamaterials less vulnerable and more resistant to structural failure. Different from the metamaterials

previously mentioned, spinodoid metamaterials are non-periodic, which enlarges their design space and contributes to the comprehensive and seamless range of anisotropic mechanical properties [7]. What's more, spinodoid metamaterials can exhibit a negative Poisson's ratio, which is advantageous for aerospace systems, such as deployable and morphing structures. In addition to the industrial applications, tailorable anisotropic elastic modulus allows spinodoid metamaterials to be applied in the medical field, e.g., patient-specific bone replacements by reproducing trabecular bone properties [7].

The critical issue in designing spinodoid metamaterials is retrieving their internal geometrical arrangements for user-defined mechanical performance. For the past decades, heuristics-based optimization approaches have been ubiquitous in the development of metamaterials, e.g., particle swarm optimization [8], genetic algorithm [9], and gradient-based approaches [10]. These approaches rely on iterative samplings and repeated computations of effective properties to search for optimal solutions with target properties. However, non-intuitive searching in a significantly vast design space [7] promised by spinodal topologies is computationally expensive. It prevents the realization of spinodoid metamaterials in engineering applications in an effective way. The recent developments in machine learning techniques have demonstrated a significant advantage in solving challenges faced in the inverse design of spinodoid metamaterials. In the work of Kumar et al. [7], a multiple-layer perceptron trained on spinodoid metamaterials bypasses expensive simulations and experiments and efficiently predicts an optimal topology for a prescribed set of mechanical properties while avoiding ill-posed inverse problems. In the work of Roding et al. [11], an appropriate Bayesian computation framework, facilitated by convolutional neural network and Gaussian random field, accelerates exploration of design space and predicts diffusivity of spinodoid metamaterials in all three directions. Although these recent studies have proposed several novel training approaches for spinodoid metamaterials for different engineering purposes, the "many-to-many" inverse problem is not addressed. In material design, the problem is to find a group of candidate geometric patterns of microstructures given a prescribed combination of on-demand effective properties. Referring to Kumar's work [7], multiple topologies of spinodoid metamaterials can contribute to identical or similar effective properties. This promotes freedom in actual fabrication by providing alternative solutions that fit manufacturing requirements.

Here, we propose an inverse design framework of 2D spinodoid metamaterials by employing a conditional generative adversarial network (CGAN) that enables the generation of a group of candidate geometric patterns with sets of target effective properties consisting of Young's modulus and shear modulus. Generative adversarial network (GAN) is one of the most popular deep learning methods because of its ability to generate fake images with many realistic characteristics [12]. The GAN frames the design problem as an unsupervised learning problem with two sub-networks, a generator and a discriminator. During the training process, the two sub-networks compete against each other to generate artificial images as authentic as images from the training dataset. Over the years, the GAN has been widely applied in metamaterial research to reveal the hidden property-structure relationship behind an extensive database [13–15]. The CGAN is the conditional or supervised version of the GAN. In the CGAN, image generation is controllable and produces

images of a given label [16]. The discriminator assesses the credibility of a fake image created by the generator based on its label of properties. The assessment process pushes the generator to produce a realistic geometric arrangement of spinodoid metamaterials. Moreover, an independent solver is applied to promote the generator to generate the arrangement with target properties. With the same input label, a well-trained generator could rapidly provide groups of candidate solutions with exact or similar target properties by modifying an input of random noise vectors from the latent space. In addition to an intuitive appearance, e.g., loss function value and training history, the performance of the CGAN is verified by checking the effective properties of the newly generated metamaterials with finite element (FE) simulations. The flowchart of the framework is illustrated in Fig. 1.

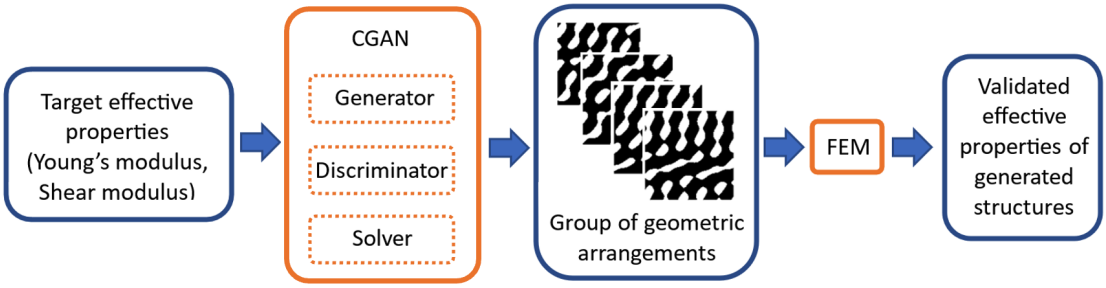

Fig. 1 Flowchart of the proposed framework: the solid and dotted orange rectangles indicate the main methodology of this framework and the sub-networks of CGAN, respectively; the solid blue rectangles indicate the inputs or outputs of the main methodology

II. Methodology

A. Definition of microstructures

The spinodoid topologies are obtained by simulating spinodal decomposition during the early phase separation stage, where homogeneous material decomposes into two phases separating materials [17]. The Cahn-Hilliard model describes the phase separation, representing the concentration fluctuation of one local phase field $\psi(x)$. Mathematically, the phase field can be described by a Gaussian random field (GRF), as a superposition of standing waves illustrated as [7]:

$$\psi(x) = \sqrt{\frac{2}{N}} \sum_{i=1}^{N>>1} \cos(\beta n_i \cdot x + \gamma_i). \tag{1}$$

Here, N is the number of the cosine waves, β is a constant wave number that is larger than zero, n_i is the uniformly distributed direction, and γ_i is the phase angle of the i^{th} wave vector. By aligning the GRF with Cartesian basis $\{\hat{e_1}, \hat{e_2}\}$, a resulting anisotropic topology of 2D spinodoid metamaterials is approximately represented in a non-uniform

orientation distribution function described by [7]:

$$n_i \sim U(\{k \in \Omega : (|k \cdot \hat{e_1}| > \cos\theta_1) \oplus (|k \cdot \hat{e_2}| > \cos\theta_2)\}), \tag{2}$$

where θ_1 and θ_2 are angles in the Cartesian coordinate system in Fig. 2(a). The angles mainly control the resulting spinodal topologies, and they are within $\theta \cup \{\theta_{min}, \frac{\pi}{2}\}$. Ω denotes a circle of unit radius in Fig. 2(a). Soyarslan et al. [18] introduced a level-set ψ_0 to generate bi-continuous solid–void microstructures by using a binary indicator function defined as:

$$X(x) = \begin{cases} 1 \ \text{(solid section)}, & \text{if } \ \psi(x) \leq \psi_0 \\ 0 \ \text{(void section)}, & \text{if } \ \psi(x) > \psi_0 \end{cases} \tag{3}$$

where $X(x)$ denotes the presence of the materials in the spinodal topologies. The binary indicator function defines the two separated phases as void and solid sections based on the threshold ϕ_0. The threshold value is related to porosity ϕ_0 of the microstructures [7]. This study considers a 2D representative volume element (RVE) for spinodoid microstructures generated by the binary indicator function. Figure 2 shows the geometric patterns of the 2D RVEs at $\phi_0 = 0.35$. A complete set of design variables $\{\theta_1, \theta_2, \phi_0\}$ characterize 2D RVEs of the spinodoid metamaterials. This study chooses $\theta_{min} = 15^\circ$ [7] and $\phi_0 = 0.35$ to guarantee that solid domains of the RVE have good structural connectivity.

Fig. 2 Spinodid topologies: (a) Schematic of the geometrical parameters: θ_1, θ_2; (b) Sample microstructures of 2D spinodoid metamaterials at $\phi_0 = 0.35$ in 128×128 pixel resolution

B. Calculation of effective properties

The target effective properties (Young's modulus and shear modulus) of spinodoid metamaterials are computed by using computational homogenization [19] via finite element method (FEM). This study chooses the base material as ULTEM® 1000, an amber transparent high-performance polyetherimide (PEI) [20]. Compared to PES (Polyethersulfone) [21], PEEK (Polyether ether ketone) [21], and Kapton (Polyimide film) [22], ULTEM 1000 is a cost-effective option with high mechanical stiffness and strength, dimensional stability, and resistance in stress cracking [23, 24]. With these outstanding features, this material can be an excellent candidate for aerospace and aircraft applications, such as interior

components [23–25]. It has isotropic elastic properties with Young's modulus of 3580 MPa and Poisson's ratio of 0.36 at room temperature [20]. Three numerical experiments are performed on the micro-scale RVE to achieve the two linear elastic moduli: one unit axial stretch imposed along each of two principal axes (Fig. 3a and 3b) and one unit shear strain imposed along both axes (Fig. 3c) [26]. Since the spinodoid topologies lack periodicity, the stress is implemented with the affine boundary condition [7]. Therefore, the resulting elastic moduli are determined by Eqs. 4 and 5, illustrated as:

$$E = \frac{\text{Normal stress}}{\text{Applied axial strain}} \tag{4}$$

$$G_{12} = \frac{\text{Shear stress}}{\text{Product of applied shear strain}} \tag{5}$$

Here, the product of the applied shear strain is the summation of transverse and longitude strains [26]. All the experiments are implemented with the finite element software, ABAQUS, and are performed under the plane stress assumption using triangular elements. Figure 4 demonstrates a sample mesh assignment of the solid section.

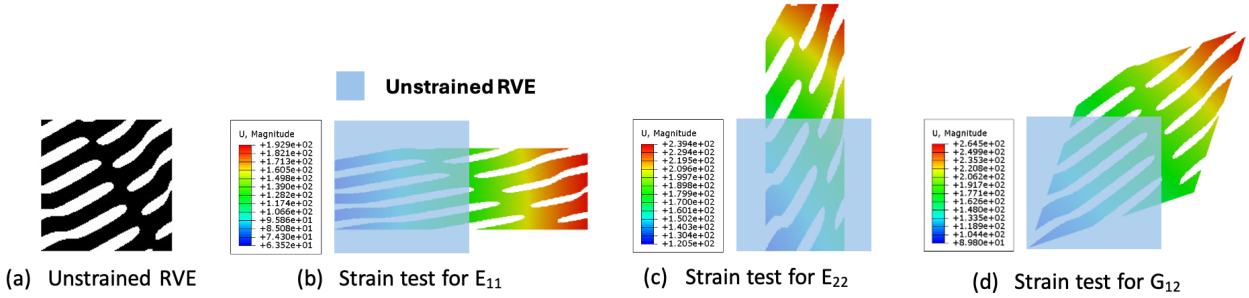

Fig. 3 Strain tests: (a) Unstrained RVE; Deformed RVEs under strain tests for (b) E_{11}, (c) E_{22}, and (d) G_{12}

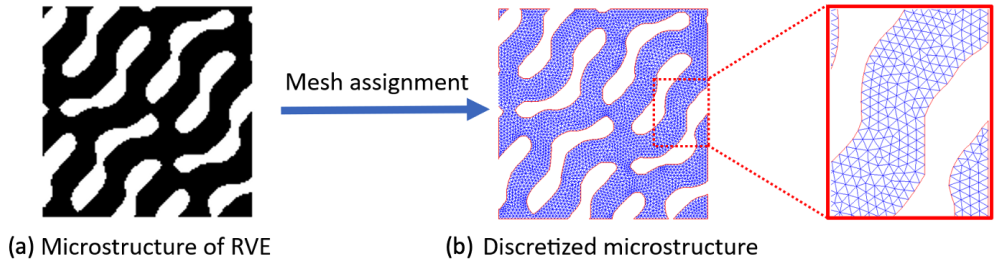

Fig. 4 Mesh assignment of 2D spinodoid metamaterials with triangular elements

C. Generation of dataset

To train the deep learning model, a dataset representing property-geometry relationships is required. The design variables are generated for spinodoid topologies using a random sampling algorithm. Once the geometric patterns of the

RVEs are obtained, their effective properties are determined by the homogenization method. In the dataset, each data point consists of a geometric pattern of the RVE and its corresponding property label (Young's modulus and shear modulus). This study converts the geometric pattern into a binary image, represented by a 128×128 element matrix. In the binary image, pixels are Boolean variables taking a value of zero for the void section or one for the solid section. Currently, the dataset contains 51,821 pairs of unique topologies and their corresponding property labels. The data domain is represented by scattering the data points in a 3D property space, with each property label on a particular axis. In Fig. 5(a), the ranges for the data domain are 1.01 MPa < E_{11} < 1588.64 MPa, 1.12 MPa < E_{22} < 2264.93 MPa, and 1.03 MPa < G_{12} < 318.75 MPa. The distributions of three properties are illustrated in Fig. 5(b). It is noticed that the ranges for Young's modulus values demonstrate a difference. This is because our microstructure generation algorithm has a bias on the spinodal topologies. The bias is mainly induced by the lower bound of design variables, θ_{min}. With the lower bound of the design variables, the generation algorithm is unable to create a geometric pattern that contains all horizontal stripes in the void section while maintaining good structural connectivity of the microstructures. Consequently, the range of E_{11} (Young's modulus in the longitudinal direction) is smaller than that of E_{22} (Young's modulus in the transverse direction). However, by rotating orientations of the microstructures, their property domain can be further expanded, which is demonstrated in the discussion. Besides, since zero values in pixels of binary images might lead to lower activation of the first layer of the network, they are replaced with "-1" in the training process [27]. For consistency with the binary images, both Young's modulus and shear modulus are normalized such that they range from -1 to 1 based on their extreme values.

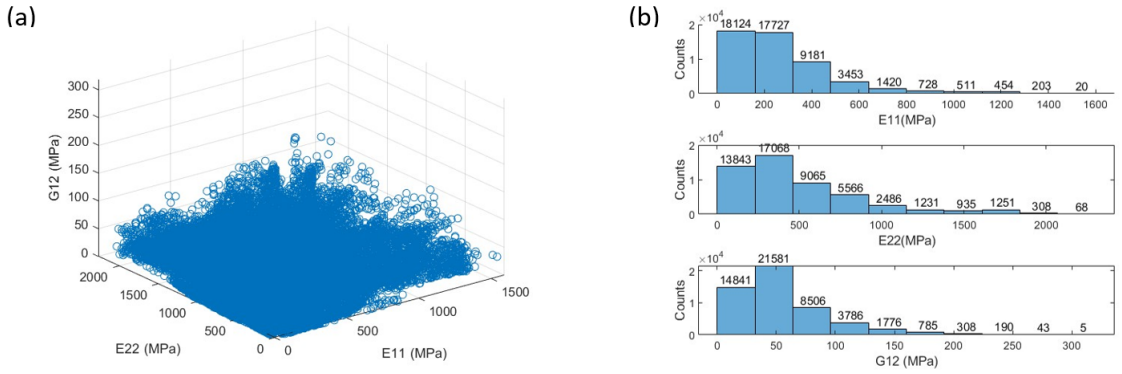

Fig. 5 Dataset for neural network training: (a) 3D property space of 51,821 randomly created data points and (b) Distributions of the property labels of CGAN for Young's modulus and shear modulus

D. Framework of inverse deep learning model

For the inverse design, this work aims to devise a CGAN to generate a group of candidate geometric patterns with effective properties that are identical or similar to target properties. The CGAN is a type of deep learning model that

achieves data generation by incorporating labels as constraints [16]. Compared to the classic GAN, the CGAN allows the users to generate images of a given type [28]. The architecture of CGAN is comprised of two sub-networks, a generator (G) and a discriminator (D). In the study, the generator takes a random noise vector from the latent space and a target property label as inputs. During the adversarial process, it learns to generate new fake geometric patterns indistinguishable from the training data for specific target properties [29]. Meanwhile, the discriminator learns to distinguish if its input of geometric patterns is real (from the training data) or fake (produced by the generator) [29]. The two networks are trained concurrently. As the discriminator identifies fake images more precisely, the generator has to generate more realistic data to fool the discriminator. However, the conventional CGAN might suffer from the overfitting problem as training the discriminator is excessively dependent on the training data [30].

To overcome this problem, an independent solver (S) promotes the generator to yield geometric patterns with objective (target) properties. The solver is a conventional neural network (CNN) applied to bridge the geometric patterns and properties (forward problem). It is a pre-trained network and independent of the two sub-networks. Training the CNN requires minimizing the mean squared error (MSE) objective function between the actual values and predictions with respect to the CNN's parameters, $\omega^{(S)}$. The objective function is defined as

$$MSE(\omega^{(S)}) = \frac{1}{N}\sum_{i=1}^{N}(y_i - \hat{y_i})^2 \tag{6}$$

where y_i is the actual property of spinodoid metamaterials, and $\hat{y_i}$ is the property predicted by the trained CNN. Consequently, the generator's parameters $\omega^{(G)}$ are updated by the discriminator and solver concurrently. The total generator loss is composed of the binary cross-entropy loss (BCE) and mean-squared error loss (MSE) of the generated microstructures. The generator loss L_G is defined as

$$L_G(\omega^{(G)}) = \frac{1}{N}\sum_{i=1}^{N}\{E_z[log(1 - D(G(z|y_i))] + \alpha(y_i - \hat{y_i})^2\} \tag{7}$$

where $\omega^{(G)}$ is the discriminator's parameters, z is the random noise vector, and α is a weighting coefficient that determines the extent to which the loss functions affect the generator. The discriminator loss is composed of the binary cross-entropy loss of the real and generated microstructures. The discriminator loss L_D is defined as

$$L_D(\omega^{(D)}) = -\frac{1}{N}\sum_{i=1}^{N}\{E_x[logD(x|y_i)] + E_z[log(1 - D(G(z|y_i))]\} \tag{8}$$

where $\omega^{(D)}$ is the discriminator's parameters and x shows the real images from the database.

A well-trained generator can create a batch of realistic binary images of spinodal topologies with sets of on-demand elastic moduli consisting of E_{11}, E_{22}, and G_{12}. Figure 6 demonstrates the general architecture of the proposed CGAN framework and summarizes the functions of the solver and discriminator. In Fig. 6, the dashed and solid lines denote

the training process of the generator updated by the discriminator and solver, respectively. In this study, the training of proposed neural networks is implemented in a Google Colab Pro system utilizing NVIDIA V100 GPUs with 32 GB memory.

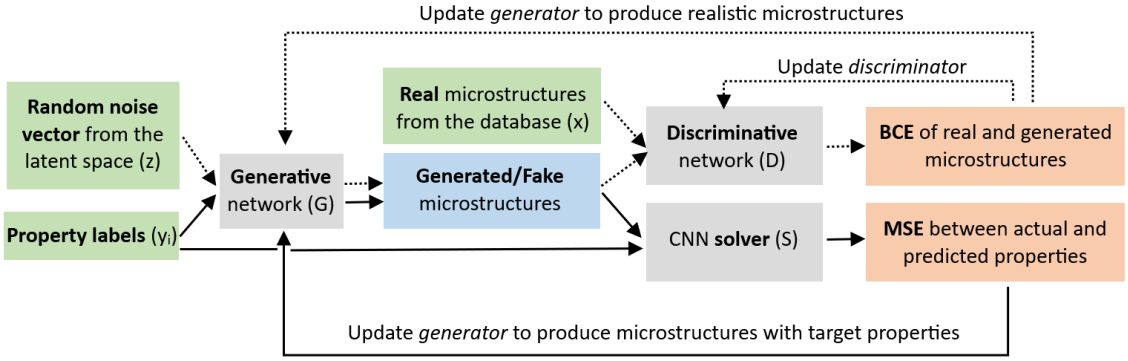

Fig. 6 General architecture of the proposed CGAN framework. The dashed and solid lines show the training process of the generator updated by the discriminator and solver, respectively.

III. Results

A. Independent convolutional solver

Since the convolutional solver is independent of the generator and discriminator, this study first processes the training on the solver with supervised learning to predict the effective properties of a given pattern in the forward direction. In Fig. 7, the solver is formed by two parts, the feature maps and the fully connected layers. The first part contains five 2D convolution layers. They extract features from an input binary image and contain 16, 32, 64, 128, and 256 channels. Max-pooling follows each convolution layer to perform down-sampling operations. The output of the feature map is flattened and directly connected with two fully connected layers containing 256 and 128 neurons. Among the 51,821 data points obtained using spinodoid topologies and FEM, 80% are randomly selected as the training dataset, and 20% are used as the test dataset. To minimize overfitting, the solver incorporates dropout layers after each fully connected layer. The early stopping strategy is utilized to further reduce model overfitting. The trainable network parameters are updated by an Adam optimizer with a learning rate of 0.0001. The training process runs for 122 epochs and the execution time is approximately 1.25 h. As shown in Fig. 8(a), the training and validation losses reach minimum values of 9.842e-4 and 9.863e-4, respectively at epoch 122. In addition to the loss, the solver's performance is statistically evaluated by the coefficient of determination (R^2) between the actual and predicted elastic moduli of 10,000 test binary images. As can be observed in Fig. 8(b)-(d), the predicted property matches the actual property relatively well for Young's moduli compared to the shear modulus. It is because of their property distribution in the database shown in Fig. 5 (b). Compared with Young's modulus, the distribution of G_{12} has a relatively large concentration in a low-value range,

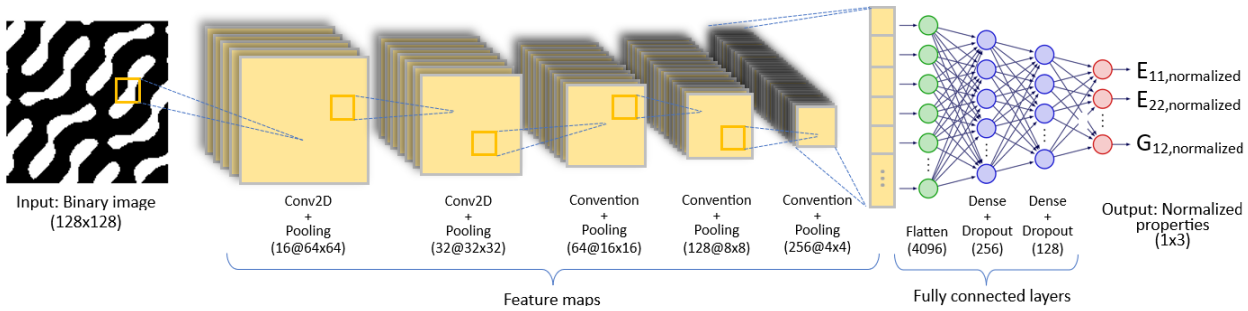

Fig. 7 Detailed architecture of CNN for the independent solvers

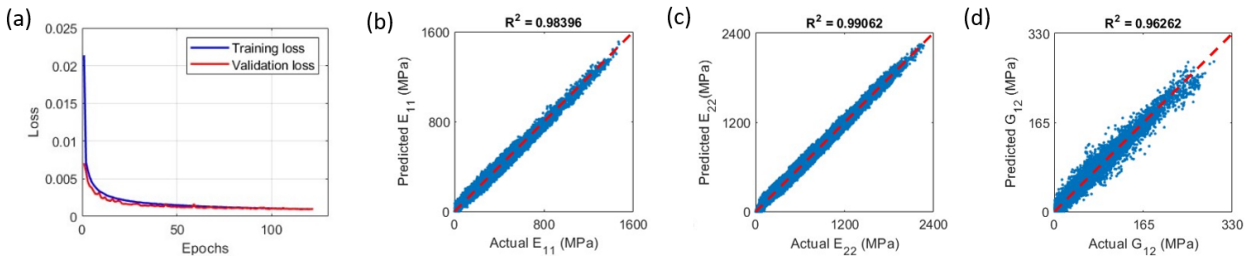

Fig. 8 Performance of the solver: (a) training history over 122 epochs, (b) (c) and (d) comparison of actual and predicted elastic moduli

leading to a relatively small amount of data points in the right tail of the distribution shown in Fig. 5(b). It induces bias in property prediction in G_{12} and a reduction in its R^2 value, which is indicated by its wider bandwidth in Fig. 8(d) compared with that of Young's modulus in Fig. 8(b) and (c). Figure 9 summarizes the history of the R^2 of G_{12} over

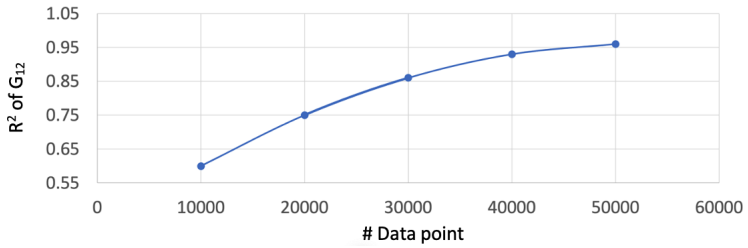

Fig. 9 History of R^2 value in G_{12} over various data sizes for training the solver

various sizes of the training data points. The figure indicates that the low accuracy in predicting values in G_{12} can be solved by enlarging the training database. However, as the number of data points increases, the growth rate of R^2 is gradually reduced. It is caused by the random sampling method for building our database. Due to the central limit theory, the data points tend to follow a Gaussian distribution, which causes them to be centrally located in a portion of the property distribution illustrated in Fig. 5. Therefore, continuously enlarging the database is an inefficient approach considering the expensive FE simulations and the gradual decrease in the growth rate of R^2. Inspired by the work of

Zheng et. al [31], the CGAN can perform importance sampling at the locations of the data distribution that contains insufficient data points. Thus, the CGAN allows us to generate new microstructures with G_{12} in a large-value range, leading to a reduction in bias in the property prediction of the networks during the training process. If the users are not satisfied with the prediction accuracy of their target properties, they can retrain the networks with a new database enriched by the CGAN. On the whole, however, the high values in R^2 (Fig. 8) indicate that our CNN solver has good performance in property predictions for the binary images of spinodoid microstructures.

B. Conditional generative adversarial network

To solve the many-to-many problem for spinodoid metamaterials, the CGAN is implemented to learn the mapping between the structural topologies and their corresponding properties. With the exception of the independent solver, our inverse deep learning model is the same as the standard CGAN, which consists of the generator and discriminator. The two neural networks are both realized as CNNs. The generator has two input channels, including 1×256 random noise vectors and a 1×3 property label. They are reshaped and concatenated into a required image format and processed through CNN with upsampling layers, 2D convolution layers, batch normalization, and leaky rectified linear unit (ReLU) activation function [32]. To be compatible with the normalized binary images (Sec. 2C), the output layer utilizes a Tanh activation function to generate new microstructures of spinodoid metamaterials represented by "-1" and "0" values in pixels. For the discriminator, a 1×3 input property label is accompanied by 128×128 input real images in the database or fake images from the generator. Two inputs of the discriminator are reshaped and processed through CNN with 2D

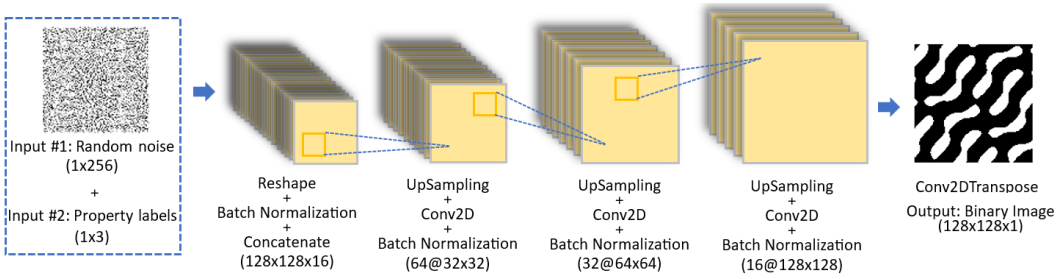

Fig. 10 Detailed architecture of the generator

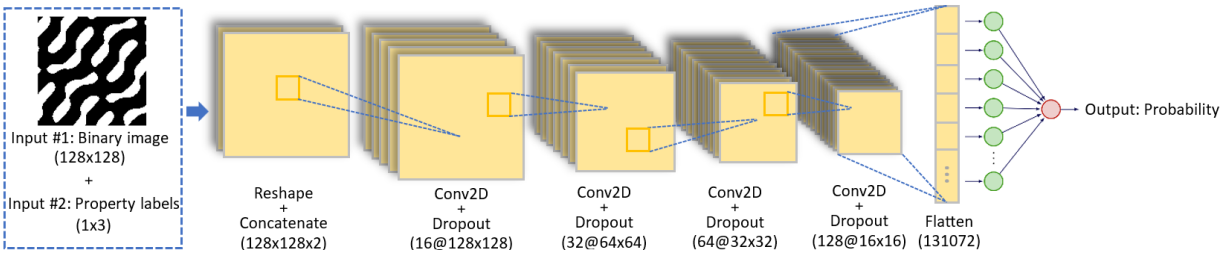

Fig. 11 Detailed architecture of the discriminator

convolution layers, a leaky ReLU activation function, and dropout layers. In its output layer, a sigmoid activation function is applied to output values in the range of 0 to 1, which indicates the probability of the sample being from realistic images. The detailed architectures of the generator and the discriminator are shown in Fig. 10 and 11, respectively.

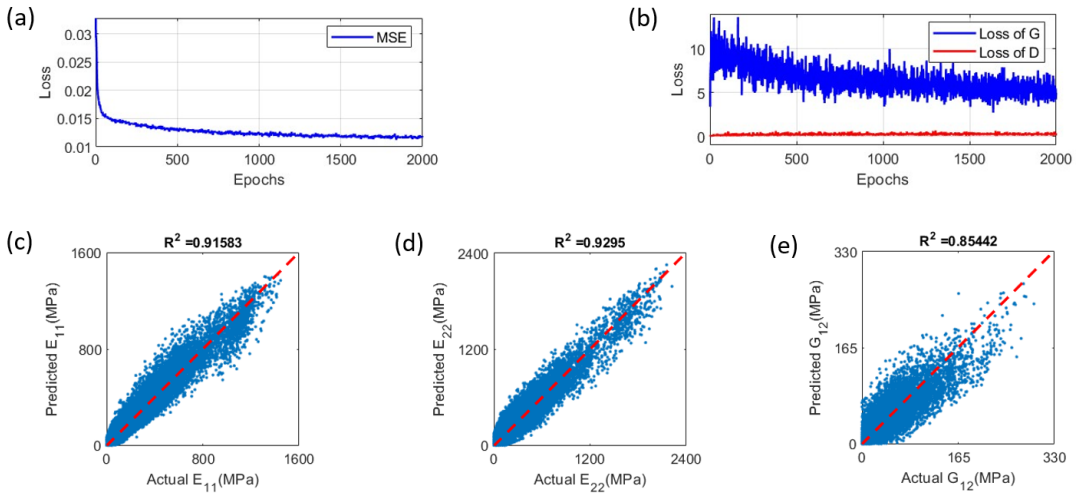

Fig. 12 Performance of the CGAN: (a) training history of the solver over 2000 epochs, (b) training history of the discriminator and generator over 2000 epochs, (c) (d) and (e) comparison of actual and predicted elastic moduli

Our proposed CGAN is trained for 2000 epochs using an Adam optimizer with a learning rate of 0.0004 and a batch size of 32. To reduce property errors between the input labels and generated images, the CGAN in the training process is mainly evaluated in terms of the MSE determined by the solver rather than the classification accuracy retrieved from the discriminator. Figures 12(a) and (b) illustrate that the losses of the generator, discriminator, and solver are minimized and stabilized after 1500 epochs of training. This indicates these networks are fully trained. There are two convergence stages in the MSE history shown in Fig. 12(a). Before epoch 70, the discriminator promotes the generator to generate realistic images, resulting in a rapid decrease in the MSE. After epoch 70, the generator is slowly updated by the solver, which progressively reduces the property errors and reaches a minimum MSE of approximately 0.012 after 1500 epochs. The large number of training epochs in the second stage indicates the relatively high difficulty in achieving the low property error compared to generating realistic images. It explains why this study employs the MSE as the major performance indicator of the CGAN. The low value in MSE indicates our trained CGAN has the capability to generate a group of realistic microstructures of spinodoid metamaterials with similar or the same user-defined Young's modulus and shear modulus. In addition, the performance of the trained CGAN is also evaluated by comparing each input/actual property and its output/predicted properties of images generated by using the CGAN. To plot actual vs predicted values of the elastic moduli, 2,000 property labels were randomly selected in the testing dataset. Our CGAN generated 10 alternative microstructures for each selected label. The plots for the resulting actual vs predicted values are shown in Fig. 12(c)-(e). In Fig. 12(c)-(e), the bandwidth of the scatter distribution for each property is wider than the

training results of the independent solver (Fig. 8(b)-(d)). It is induced by outliers of the alternative microstructures with large property errors. But in general, the scattered points distribute closely along the bisection line. It represents our CGAN is capable of generating alternative microstructures with similar or the same properties as the input properties. Among the elastic moduli, the coefficient of determination of G_{12} becomes much smaller compared to the training results of the independent solver. It is due to the error propagation from the solver and the lack of data points in the training dataset of G_{12}. An extensive database allows the CGAN to explore the implicit property-geometry relations more accurately. However, the higher performance of the CGAN requires additional runs of the FE simulation and training process, which are both time-consuming. Thus, by considering the trade-off between efficiency and accuracy in our CGAN, the values of the R^2 in Fig. 12 are acceptable.

IV. Discussion

A. Inverse design of spinodoid metamaterials

After assessing the performance of the CGAN, this section utilizes our trained CGAN to perform the inverse design of spinodoid metamaterials. User-defined property labels are the inputs of the CGAN to generate a batch of microstructures with the corresponding elastic moduli. To demonstrate the capacity of our CGAN to enrich data points on the right tail of the histogram in Fig. 5(b), property labels are selected and include at least one elastic modulus with a large value. Fig. 13 shows sample alternative microstructures for each selected property label of [E_{11}, E_{22}, G_{12}], including [1251.4, 302.4, 45.6] MPa, [97.1, 965.7, 25.6] MPa, and [342.6, 513.2, 175.6] MPa. To select an appropriate microstructure among these alternative solutions, the users are required to make a trade-off between accuracy in their corresponding properties and uncertainty in the structural dimension during the additive manufacturing process. Similar to the importance sampling, Fig. 14 demonstrates that our CGAN is able to enrich the database in the right tail of its histogram with new 20,000 data points in an efficient way. Compared to the randomly generated method, our proposed inverse design framework does not require spinodoid topologies with geometrical design parameters and property calculations by finite element method (FEM). Note that the distribution of shear modulus for CGAN-outputted patterns with an input G_{12} = 150.6 MPa is left-skewed in Fig. 14(c) due to the highly concentrated data points on the low values of the shear modulus in the training database.

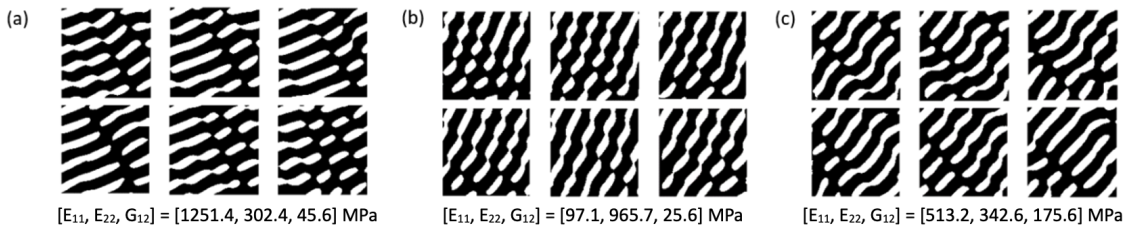

Fig. 13 Sample alternative microstructures with three different input property labels of the CGAN

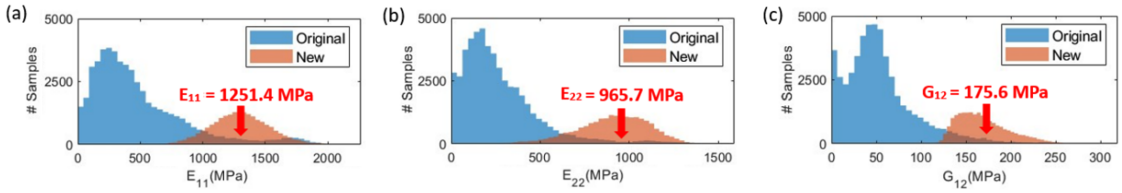

Fig. 14 Distributions of elastic moduli from the original database and from the newly generated samples with an input condition of (a) E_{11} = 965.7 MPa, (b) E_{22} = 1251.4 MPa, and (c) G_{12} = 175.6 MPa

To validate the microstructures generated by the CGAN, this study performs FE simulations of the generated microstructures in accordance with the FEM model in Sec. 2B. Table 1 summarizes the validation results of sample microstructures covering wide ranges of corresponding properties. The results include input property labels of the generator, predicted properties of generated microstructures (pre-trained solver), and actual properties of generated microstructures (FE simulation). Since the CGAN employs the MSE of the solvers as part of its loss function, the difference between the input labels and predicted properties is relatively small compared to the actual properties. Owing to the distribution of the training dataset, the difference increases as the values of the elastic moduli increase. In general, the small difference among the validated results for each input label indicates that both the CNN solver and the CGAN have a good performance in mapping property-geometry relations in a forward and inverse fashion, respectively.

Table 1 Validation results of spinodoid microstructures generated by CGAN

Case #	1	2	3	4	5	6
Spinodoid microstructures generated by CGAN						
E_{11}(input), MPa	1248.60	386.30	98.50	513.60	662.30	199.50
E_{11}(CNN), MPa	1249.50	386.03	98.68	514.17	662.96	199.38
E_{11}(FEM), MPa	1251.06	385.44	98.88	515.30	664.00	199.24
E_{22}(input), MPa	76.20	1911.20	960.30	1225.90	393.40	685.90
E_{22}(CNN), MPa	76.34	1912.66	959.29	1224.99	393.64	686.56
E_{22}(FEM), MPa	76.51	1915.28	957.64	1223.31	393.94	687.74
G_{12}(input), MPa	20.73	50.17	72.08	132.00	160.86	201.62
G_{12}(CNN), MPa	20.58	50.42	72.58	131.08	158.93	204.04
G_{12}(FEM), MPa	20.38	50.77	73.29	129.78	157.19	206.22

B. Mechanical behavior of spinodoid metamaterials

In our 2D study case, the resulting mechanical behavior of spinodoid metamaterials is represented as a second-order homogenized elastic modulus tensor $\hat{C}_{ij} = [C_{11}, C_{12}, C_{13}; C_{21}, C_{22}, C_{23}; C_{31}, C_{32}, C_{33}]$. The modulus tensor is linearly elastic and obtained by applying average strain $\overline{\varepsilon}_{ij}$ on the RVEs, computing the volume-averaged stress $\overline{\sigma}_{ij}$ by FE

simulations, and solving the stress-strain relationship defined as $\overline{\sigma}_{ij} = \hat{C}_{ij}\overline{\varepsilon}_{ij}$. To further expand the design space, the orientation of materials is manipulated to explore structures with outstanding properties. The anisotropic Young's modulus distribution along all directions d in the Cartesian coordinates is computed by the equation defined as $E(d) = (\sum_{i,j=1}^{2} \hat{C}_{ij}^{-1} d_i d_j)^{-1}$ [7]. Table 2 summarizes the resulting anisotropic Young's modulus of five representative microstructures. The longitudinal and transverse axes correspond to normalized E_{11} and E_{22}, respectively.

Table 2 Anisotropic homogenized Young's modulus of the microstructures generated by CGAN

Case #	1	2	3	4	5
Spinodoid microstructures generated by CGAN					
Anisotropic properties of Young's modulus		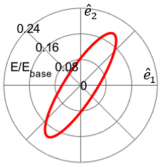			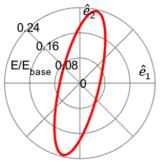

Moreover, this study performs tensile tests and FE simulations to further explore the mechanical behavior of spinodoid metamaterials under a small deformation with a strain ε of 0.03. Table 3 summarizes the displacement fields of the selected microstructures under the uniaxial tensile tests in two principal directions. With the displacement fields achieved from ABAQUS, the axial and lateral changes in the displacement of microstructures are calculated using MATLAB. The Poisson's ratio is calculated by the engineering strains, which are derived from the averaged displacements [33]. In Table 3, the overall deformation findings prove that our tailored metamaterials can retrieve a negative Poisson's ratio, which is advantageous for aerospace systems, such as deployable and morphing structures.

Table 3 Displacement fields of the microstructures generated by CGAN

Case #	Spinodoid microstructures generated by CGAN	**Displacement field of uniaxial tensile test**	
		Longitudinal direction (X)	Transverse direction (Y)
1		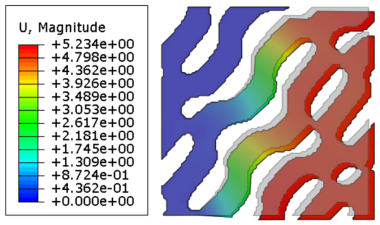	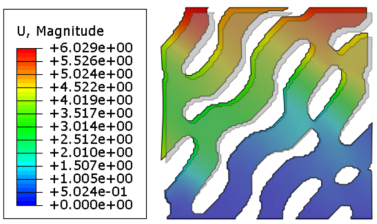

Table 3 **Displacement fields of the microstructures generated by CGAN (continued)**

Case #	Spinodoid microstructures generated by CGAN	Displacement field of uniaxial tensile test	
		Longitudinal direction (X)	Transverse direction (Y)
2		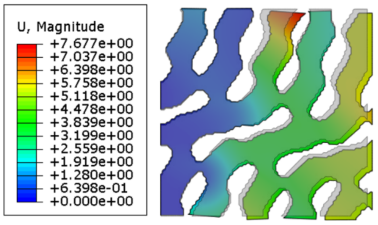	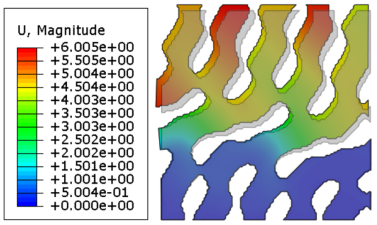
3		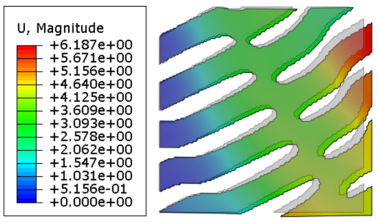	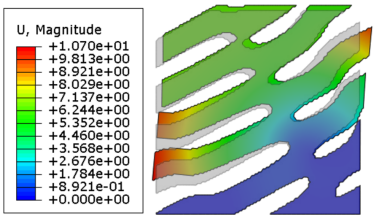
4		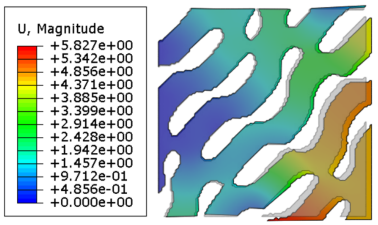	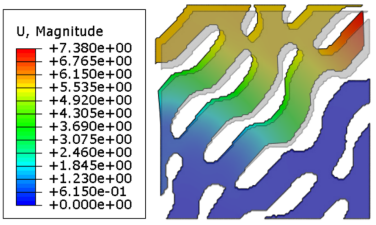
5		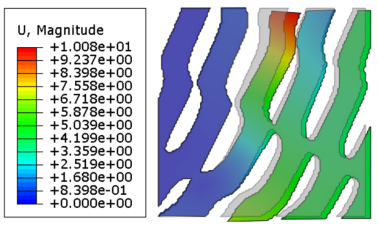	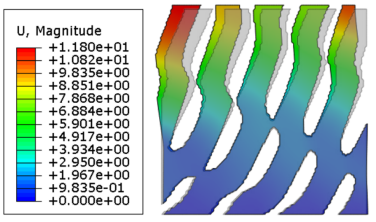

Table 4 **Poisson's ratio values of the microstructures from Table 3**

Case #	1	2	3	4	5
Poisson's ratio, ν_{12}	-0.3010	0.0346	0.2551	-0.0953	0.2155
Poisson's ratio, ν_{21}	-0.0908	0.0288	0.3682	-0.0875	0.1254

V. Conclusion

We propose a framework based on CGANs to perform the inverse design of 2D spinodoid metamaterials. The developed CGAN framework leverages a pre-trained independent solver to facilitate our deep-learning network and achieve accurate predictions for highly nonlinear property-geometry relations. To address the inverse design problem, the proposed framework realizes microstructures with user-defined Young's modulus and shear modulus values. Once it is

well-trained, the deep-learning network can bypass numerical simulations and accelerate the tailoring of microstructures to achieve various desired properties. With our CGAN framework, users can obtain a batch of optimal designs targeting elastic moduli in a highly efficient way. These designs are alternative solutions to the many-to-many problems and promote high freedom in the fabrication process. The results of our framework for mechanical behavior confirm that the presented 2D spinodoid metamaterials have superior features, including negative Poisson's ratio and an extensive design space with anisotropic properties. Although the results of this study are based on a specific dataset for spinodoid metamaterials with a particular porosity, the same framework can be extended to design other metamaterials with microstructures represented by binary images (e.g. porous metamaterials [34], truss metamaterials [35], and chiral metamaterials [36]). Considering the wide application of spinodoid metamaterials [7, 11], our design framework is not limited to ULTEM 1000 and its base material can be replaced with various materials for specific applications, such as ultra-high molecular weight polyethylene (UHMWPE) for bone replacement [37] and Polylactic acid (PLA) for energy absorption [38]. Future work will concentrate on the inverse design of 3D spinodoid metamaterials using CGANs facilitated with 3D CNNs.

Funding

This research was supported by the National Science Foundation (NSF) CMMI Division Grant CMMI-2053840 and NSF CAREER Award CMMI-2236947 (Program Director: Dr. Kathryn Jablokow).

Acknowledgement

The authors would like to acknowledge the assistance provided by Dr. Sadik Omairey in sharing the ABAQUS CAE interface plugin (EasyPBC).

References

[1] Tay, Y. Y., Lim, C. S., & Lankarani, H. M. (2014). A finite element analysis of high-energy absorption cellular materials in enhancing passive safety of road vehicles in side-impact accidents. In International Journal of Crashworthiness (Vol. 19, Issue 3, pp. 288–300). Informa UK Limited. https://doi.org/10.1080/13588265.2014.893789

[2] Benedetti, M., du Plessis, A., Ritchie, R. O., Dallago, M., Razavi, S. M. J., & Berto, F. (2021). Architected cellular materials: A review on their mechanical properties towards fatigue-tolerant design and fabrication. In Materials Science and Engineering: R: Reports (Vol. 144, p. 100606). Elsevier BV. https://doi.org/10.1016/j.mser.2021.100606

[3] du Plessis, A., Razavi, S. M. J., Benedetti, M., Murchio, S., Leary, M., Watson, M., Bhate, D., & Berto, F. (2022). Properties and applications of additively manufactured metallic cellular materials: A review. In Progress in Materials Science (Vol. 125, p. 100918). Elsevier BV. https://doi.org/10.1016/j.pmatsci.2021.100918

[4] Neville, R. M., Scarpa, F., & Pirrera, A. (2016). Shape morphing Kirigami mechanical metamaterials. In Scientific Reports (Vol. 6, Issue 1). Springer Science and Business Media LLC. https://doi.org/10.1038/srep31067

[5] Kenanakis, G., Zhao, R., Stavrinidis, A., Konstantinidis, G., Katsarakis, N., Kafesaki, M., Soukoulis, C. M., & Economou, E. N. (2012). Flexible chiral metamaterials in the terahertz regime: a comparative study of various designs. In Optical Materials Express (Vol. 2, Issue 12, p. 1702). The Optical Society. https://doi.org/10.1364/ome.2.001702

[6] Mizzi, L., Mahdi, E. M., Titov, K., Gatt, R., Attard, D., Evans, K. E., Grima, J. N., & Tan, J.-C. (2018). Mechanical metamaterials with star-shaped pores exhibiting negative and zero Poisson's ratio. In Materials & Design (Vol. 146, pp. 28–37). Elsevier BV. https://doi.org/10.1016/j.matdes.2018.02.051

[7] Kumar, S., Tan, S., Zheng, L., & Kochmann, D. M. (2020). Inverse-designed spinodoid metamaterials. In npj Computational Materials (Vol. 6, Issue 1). Springer Science and Business Media LLC. https://doi.org/10.1038/s41524-020-0341-6

[8] He, L., Lin, Z., Wen, Y., Chen, Y., & Yu, S. (2020). An Inverse Design Method Combining Particle Swarm Optimization and Wavefront Matching Method for Multiplane Light Conversion. In Frontiers in Optics / Laser Science. Frontiers in Optics. Optica Publishing Group. https://doi.org/10.1364/fio.2020.fm7d.5

[9] Liu, S., & Acar, P. (2022). Inverse Multiscale Design of Cellular Mechanical Metamaterials. In AIAA SCITECH 2022 Forum. AIAA SCITECH 2022 Forum. American Institute of Aeronautics and Astronautics. https://doi.org/10.2514/6.2022-1135

[10] Oliveri, G., & Overvelde, J. T. B. (2020). Inverse Design of Mechanical Metamaterials That Undergo Buckling. In Advanced Functional Materials (Vol. 30, Issue 12, p. 1909033). Wiley. https://doi.org/10.1002/adfm.201909033

[11] Röding, M., Wåhlstrand Skärström, V., & Lorén, N. (2022). Inverse design of anisotropic spinodoid materials with prescribed diffusivity. In Scientific Reports (Vol. 12, Issue 1). Springer Science and Business Media LLC. https://doi.org/10.1038/s41598-022-21451-6

[12] Creswell, A., White, T., Dumoulin, V., Arulkumaran, K., Sengupta, B., & Bharath, A. A. (2018). Generative Adversarial Networks: An Overview. In IEEE Signal Processing Magazine (Vol. 35, Issue 1, pp. 53–65). Institute of Electrical and Electronics Engineers (IEEE). https://doi.org/10.1109/msp.2017.2765202

[13] Gurbuz, C., Kronowetter, F., Dietz, C., Eser, M., Schmid, J., & Marburg, S. (2021). Generative adversarial networks for the design of acoustic metamaterials. In The Journal of the Acoustical Society of America (Vol. 149, Issue 2, pp. 1162–1174). Acoustical Society of America (ASA). https://doi.org/10.1121/10.0003501

[14] Challapalli, A., Patel, D., & Li, G. (2021). Inverse machine learning framework for optimizing lightweight metamaterials. In Materials & Design (Vol. 208, p. 109937). Elsevier BV. https://doi.org/10.1016/j.matdes.2021.109937

[15] Lin, H., Tian, Y., Hou, J., Xu, W., Shi, X., & Tang, R. (2022). Fussy Inverse Design of Metamaterial Absorbers Assisted by a Generative Adversarial Network. In Frontiers in Materials (Vol. 9). Frontiers Media SA. https://doi.org/10.3389/fmats.2022.926094

[16] Mirza, M., & Osindero, S. (2014). Conditional Generative Adversarial Nets (Version 1). arXiv. https://doi.org/10.48550/ARXIV.1411.1784

[17] Cahn, J. W., & Hilliard, J. E. (1958). Free Energy of a Nonuniform System. I. Interfacial Free Energy. In The Journal of Chemical Physics (Vol. 28, Issue 2, pp. 258–267). AIP Publishing. https://doi.org/10.1063/1.1744102

[18] Soyarslan, C., Bargmann, S., Pradas, M., & Weissmüller, J. (2018). 3D stochastic bicontinuous microstructures: Generation, topology and elasticity. In Acta Materialia (Vol. 149, pp. 326–340). Elsevier BV. https://doi.org/10.1016/j.actamat.2018.01.005

[19] Huet, C. (1990). Application of variational concepts to size effects in elastic heterogeneous bodies. In Journal of the Mechanics and Physics of Solids (Vol. 38, Issue 6, pp. 813–841). Elsevier BV. https://doi.org/10.1016/0022-5096(90)90041-2

[20] SABIC Innovative Plastics ULTEM 1000R PEI, http://www.lookpolymers.com/polymer_SABIC-Innovative-Plastics-ULTEM-1000R-PEI.php. Accessed March 18, 2020.

[21] Kutz, M. (2023). Applied Plastics Engineering Handbook: Processing, sustainability, materials, and applications. William Andrew.

[22] Inagaki, M., Harada, S., Sato, T., Nakajima, T., Horino, Y., & Morita, K. (1989). Carbonization of polyimide film "Kapton." In Carbon (Vol. 27, Issue 2, pp. 253–257). Elsevier BV. https://doi.org/10.1016/0008-6223(89)90131-0

[23] Ultem 1000. Emco Plastics. https://www.emcoplastics.com/ultem-1000/. Accessed Jan. 6, 2023

[24] Ultem use in Aerospace Applications. Performance Plastics. https://performanceplastics.com/blog/ultem-use-in-aerospace-applications/. Accessed Jan. 6, 2023

[25] Kafi, A., Wu, H., Langston, J., Atak, O., Kim, H., Kim, S., Fahy, W. P., Reber, R., Misasi, J., Bateman, S., & Koo, J. H. (2020). Evaluation of additively manufactured ultraperformance polymers to use as thermal protection systems for spacecraft. In Journal of Applied Polymer Science (Vol. 137, Issue 37). Wiley. https://doi.org/10.1002/app.49117

[26] Omairey, S. L., Dunning, P. D., & Sriramula, S. (2018). Development of an ABAQUS plugin tool for periodic RVE homogenization. In Engineering with Computers (Vol. 35, Issue 2, pp. 567–577). Springer Science and Business Media LLC. https://doi.org/ 10.1007/s00366-018-0616-4

[27] Gurbuz, C., Kronowetter, F., Dietz, C., Eser, M., Schmid, J., & Marburg, S. (2021). Generative adversarial networks for the design of acoustic metamaterials. In The Journal of the Acoustical Society of America (Vol. 149, Issue 2, pp. 1162–1174). Acoustical Society of America (ASA). https://doi.org/10.1121/10.0003501

[28] Isola, P., Zhu, J.-Y., Zhou, T., & Efros, A. A. (2017). Image-to-Image Translation with Conditional Adversarial Networks. In 2017 IEEE Conference on Computer Vision and Pattern Recognition (CVPR). 2017 IEEE Conference on Computer Vision and Pattern Recognition (CVPR). IEEE. https://doi.org/10.1109/cvpr.2017.632

[29] Creswell, A., White, T., Dumoulin, V., Arulkumaran, K., Sengupta, B., & Bharath, A. A. (2018). Generative Adversarial Networks: An Overview. In IEEE Signal Processing Magazine (Vol. 35, Issue 1, pp. 53–65). Institute of Electrical and Electronics Engineers (IEEE). https://doi.org/10.1109/msp.2017.2765202

[30] Lee, M., & Seok, J. (2017). Controllable Generative Adversarial Network (Version 5). arXiv. https://doi.org/10.48550/ARXIV.1708.00598

[31] Zheng, X., Chen, T.-T., Guo, X., Samitsu, S., & Watanabe, I. (2021). Controllable inverse design of auxetic metamaterials using deep learning. In Materials & Design (Vol. 211, p. 110178). Elsevier BV. https://doi.org/10.1016/j.matdes.2021.110178

[32] Agarap, A. F. (2018). Deep Learning using Rectified Linear Units (ReLU) (Version 2). arXiv. https://doi.org/10.48550/ARXIV.1803.08375

[33] Alomarah, A., Masood, S. H., & Ruan, D. (2022). Metamaterials with enhanced mechanical properties and tuneable Poisson's ratio. In Smart Materials and Structures (Vol. 31, Issue 2, p. 025026). IOP Publishing. https://doi.org/10.1088/1361-665x/ac3c08

[34] Librandi, G., Moshe, M., Lahini, Y., & Bertoldi, K. (2017). Porous mechanical metamaterials as interacting elastic charges. arXiv: Soft Condensed Matter.

[35] Glaesener, R. N., Bastek, J.-H., Gonon, F., Kannan, V., Telgen, B., Spöttling, B., Steiner, S., & Kochmann, D. M. (2021). Viscoelastic truss metamaterials as time-dependent generalized continua. In Journal of the Mechanics and Physics of Solids (Vol. 156, p. 104569). Elsevier BV. https://doi.org/10.1016/j.jmps.2021.104569

[36] Wu, W., Hu, W., Qian, G., Liao, H., Xu, X., & Berto, F. (2019). Mechanical design and multifunctional applications of chiral mechanical metamaterials: A review. In Materials & Design (Vol. 180, p. 107950). Elsevier BV. https://doi.org/10.1016/j.matdes.2019.107950

[37] Senra, M. R., & Marques, M. de F. V. (2020). Synthetic Polymeric Materials for Bone Replacement. In Journal of Composites Science (Vol. 4, Issue 4, p. 191). MDPI AG. https://doi.org/10.3390/jcs4040191

[38] Yazdani Sarvestani, H., Akbarzadeh, A. H., Niknam, H., & Hermenean, K. (2018). 3D printed architected polymeric sandwich panels: Energy absorption and structural performance. In Composite Structures (Vol. 200, pp. 886–909). Elsevier BV. https://doi.org/10.1016/j.compstruct.2018.04.002